**Research
Article**

Dynamic Stall Modelling of the S809 Aerofoil and Comparison with Experiments

Sandeep Gupta and J. Gordon Leishman*, Department of Aerospace Engineering, University of Maryland, College Park, MD 20742, USA

An analysis of dynamic stall for the S809 aerofoil has been performed in conjunction with the Leishman–Beddoes dynamic stall model that was modified for wind turbine applications. Numerical predictions of the lift, drag and pitching moment coefficients were compared with measurements obtained for an oscillating S809 aerofoil at various reduced frequencies, mean angles of attack and angle of attack amplitudes. It was found that the results using the modified model were in good agreement with the experimental data. Hysteresis in the aerodynamic coefficients was captured well, although the drag coefficient was slightly underpredicted in the deep stall flow regime. Validation against the experimental data showed overall good agreement. The mathematical structure of the model is such that it can be readily incorporated into a comprehensive analysis code for a wind turbine. Copyright © 2006 John Wiley & Sons, Ltd.

Introduction

The successful prediction of the unsteady blade loads and power output of wind turbines is very important for designing low-cost and reliable wind turbines.[1,2] Understanding wind turbine aerodynamics[3] in all working states is one of the key factors in making improved predictions of their performance. The flow field associated with wind turbines is highly three-dimensional and unsteady in nature and as of yet is not well understood.[1,4] The operation of wind turbines at power settling along with unsteady effects such as atmospheric turbulence, the ground boundary layer, directional and spatial variations in wind shear, yawed flow and wind gusts, as well as the effects of an upstream support structure (tower shadow),[5] compounds the difficulties in accurate prediction of the flow field at the turbine disc.

Wind turbine blade sections can operate with stall at low tip speed ratios and can undergo dynamic stall during operation in yawed flow. Because of the low rotational speed of a turbine, the inboard regions of the blades are stalled for much of their operational time. Additionally, stall regulation is one of the methods used to control peak power output for smaller wind turbines. For larger wind turbines, which use pitch control for power regulation, stall conditions can occur during wind gusts. Thus predicting blade loads and the power output during stall (and in the post-stall region) is fundamental to the improved design of all types of wind turbines.

* Correspondence to: J. G. Leishman, Department of Aerospace Engineering, 3181 Glenn L. Martin Institute of Technology, University of Maryland, College Park, MD 20742, USA.
Email: leishman@eng.umd.edu

WILEY
InterScience®
DISCOVER SOMETHING GREAT

An aerofoil section undergoes dynamic stall[6] when it is subjected to any form of unsteady angle of attack motion (pitching, plunging, etc.), which takes the effective angle of attack beyond its normal static stall angle. Dynamic stall of an aerofoil is characterized by the shedding of a strong vortical disturbance from its leading edge, which is called a dynamic stall vortex. The onset of flow separation is also delayed to an angle of attack higher than the static stall angle and, combined with the effects of the dynamic stall vortex, is responsible for elevated values of lift. The aft movement of the centre of pressure during the vortex shedding causes a large nose-down pitching moment (moment stall). When the angle of attack decreases, flow reattachment is found to be delayed to an angle of attack lower than the static stall angle. This leads to significant hysteresis in the air loads and reduced aerodynamic damping, particularly in torsion.[7] This can cause torsional aeroelastic instabilities on the blades. Therefore the consideration of dynamic stall is important to predict the unsteady blade loads and also to define the operational boundaries of a wind turbine.

Modelling of dynamic stall through the numerical solution of the unsteady Navier–Stokes equations with CFD techniques has shown some recent success,[8,9] and has become increasingly feasible with the increase in computational power. CFD solutions are, however, still computationally very expensive and are basically prohibitive for the routine engineering analyses of wind turbines. In addition, there are numerous issues such as turbulence modelling that still need to be understood. In the absence of less approximate and cost-effective solutions, researchers have used various semi-empirical models to represent dynamic stall.[10–13] See Reference 14 for a discussion on dynamic stall and alternative models. The advantage of using these models is their relative simplicity and low computational expense. These models have met with good success and have been shown to improve the predictive capability for blade air loads. Some of these models have also been used for wind turbine applications.[15,16]

In this study a version of the Leishman–Beddoes (L–B) dynamic stall model[11] has been used to predict the aerodynamic characteristics of the S809 aerofoil under incipient and deep dynamic stall conditions. Several key modifications have been made to the base model to improve its validity over a wider range of angle of attack and operating Reynolds numbers representative of wind turbines. The term 'modified L–B model' represents the static and dynamic stall model together. The S809 aerofoil has very different aerofoil characteristics compared with helicopter sections for which the L–B model was originally developed; this aerofoil is designed to have pronounced trailing edge flow separation, and its modelling requires several modifications to the representation of the static stall model. The success of the L–B dynamic stall model is dependent on accurate representation of the static coefficients. The numerical predictions are then validated against measurements for the S809 aerofoil.[17] The present study is an important step towards validating a coupled free vortex wake[18,19] and blade model for the general analysis of wind turbine aerodynamics.[20]

Methodology

The authors have tried to minimize the details on the methodology of the L–B model. However, in the wind turbine community there is clearly a lack of understanding of the model and its application. Most of this section describes both the static and unsteady models. This is essential because the proper representation of the static characteristics is very important for the success of the L–B model.

Unsteady Attached Flow

The mathematical root of the L–B model lies within the classical, incompressible unsteady thin aerofoil theory, but it is modified semi-empirically to represent subsonic flow effects. The ability to accurately predict the unsteady aerodynamic forces and moments in attached flows is critical to the prediction of the onset of nonlinear aerodynamic effects such as dynamic stall. The unsteady attached flow response is computed in the L–B model in terms of a superposition of indicial aerodynamic responses. The indicial functions were derived for the Mach number range appropriate to helicopter rotors, but they can be applied to lower Mach numbers as well. The indicial responses are composed of the non-circulatory and circulatory loading components, which are written in functional form as exponential series. For a continuously changing angle of attack the effective

unsteady angle of attack of the aerofoil is given by

$$\alpha_e^c(s, M) = \alpha(s) - X(s) - Y(s) \tag{1}$$

where $X(s)$ and $Y(s)$ are deficiency functions written in terms of the exponential series representation of the indicial functions as given by

$$X(s) = A_1 \int_{s_0}^{s} \frac{d\alpha}{ds}(\sigma) \exp[-b_1(s-\sigma)d\sigma] \tag{2}$$

$$Y(s) = A_2 \int_{s_0}^{s} \frac{d\alpha}{ds}(\sigma) \exp[-b_2(s-\sigma)d\sigma] \tag{3}$$

These integral equations can be solved using a special finite difference approximation to Duhamel's integral that is formulated as a set of recurrence equations. A second-order algorithm can be written as

$$X(s) = X(s-\Delta s)\exp(-b_1\beta^2\Delta s) + A_1\Delta\alpha\exp(-b_1\beta^2\Delta s/2) \tag{4}$$

$$Y(s) = Y(s-\Delta s)\exp(-b_2\beta^2\Delta s) + A_2\Delta\alpha\exp(-b_2\beta^2\Delta s/2) \tag{5}$$

Here A_1, A_2, b_1 and b_2 are the coefficients of indicial functions and are a function of the aerofoil and the Mach number. These recurrence relations account for the circulatory time history effects in the air loads. A similar recurrence relation is used for the non-circulatory part of the air loads (see References 11 and 12 for details). This linear unsteady aerodynamic model then forms the root for the upper-level part of the overall non-linear aerodynamic model (as shown later in Figure 3).

Unsteady Separated Flow

Defining the onset of leading edge flow separation is the most important aspect of modelling dynamic stall. The criterion in the L–B model for static leading edge flow separation can be represented in terms of the critical leading edge pressure and the associated pressure gradient. This is equivalent to defining a critical value of normal force coefficient, C_{n_1}, which corresponds to the critical pressure for the onset of flow separation.[10] Under unsteady conditions there is a lag in the leading edge pressure with increasing angle of attack, which can be expressed as a first-order lag as given by

$$C_n' = C_n - D_n^p \tag{6}$$

where D_n^p is given by

$$D_{n_k}^p = D_{n_{k-1}}^p \exp\left(-\frac{\Delta s}{T_p}\right) + (C_{n_k}^p - C_{n_{k-1}}^p)\exp\left(-\frac{\Delta s}{2T_p}\right) \tag{7}$$

The attainment of $C_n' \geq C_{n_1}$ causes leading edge flow separation. The time constant T_p is determined from unsteady aerofoil data. Based on correlation with various aerofoils, T_p has been found to be largely independent of aerofoil shape.[11,21]

Trailing edge flow separation causes a loss of circulation and introduces non-linearities into the lift, drag and pitching moment. To represent the static (quasi-steady) non-linear post-stall behaviour, the Kirchhoff/Helmholtz formulation[22,23] for modelling the lift on a flat plate is used. The relationship between the normal force coefficient and a fixed trailing edge flow separation point is given by

$$C_n^f = C_{n\alpha}\left(\frac{1+\sqrt{f}}{2}\right)^2 \alpha \tag{8}$$

where f is the location of the effective flow separation point non-dimensionalised by the chord length ($f = x/c$). This formulation is strictly valid only up to moderate angles of attack. To model the aerofoil behaviour at high angles of attack, such as may be seen in wind turbines, the equation is modified to read

$$C_n^f = C_{n_\alpha} \left(\frac{1 + \sqrt{f}}{2} \right)^2 \sin \alpha \tag{9}$$

The variation of the effective separation point f with angle of attack α can be obtained from experimental measurements of the static C_n by rearranging equation (9) to solve for f in terms of the measured C_n and α.

It is, however, not possible to define a general expression for the pitching moment variation from the Kirchhoff formulation, so an empirical relation must be used. This relation is derived from static aerofoil measurements by expressing the centre of pressure variation C_m/C_n as a function of the effective flow separation point.[12] The empirical relation for C_m/C_n (accounting for the zero-lift moment) for the S809 aerofoil is fitted to the form

$$C_m = \begin{cases} C_{m_0} + [C_0 + C_1(1-f) + C_2 \sin(\pi f^m)]C_n, & \alpha < \alpha_2 \\ C_{m_0} + [C_0 + C_1 \exp(C_2 f^m)]C_n, & \alpha > \alpha_2 \end{cases} \tag{10}$$

Here C_{m_0} is the zero-lift moment and C_0 is the mean offset of the aerodynamic centre from the $\frac{1}{4}$-chord ($C_0 = x_{ac}/c - \frac{1}{4}$). The coefficients C_1 and C_2 describe the non-linear variation of the centre of pressure. Figure 1 shows the variation of the steady centre of pressure for the S809 aerofoil *versus* the separation point f, and Figure 2 shows the reconstructed pitching moment curve according to equation (10).

Under unsteady flow conditions the value of f is modified because of the previously mentioned temporal effects on the aerofoil pressure distribution and the boundary layer response. The effective angle of attack after incorporating the unsteady pressure response is given by

$$\alpha_f = C_n'/C_{n_\alpha} \tag{11}$$

This value of α_f is used to obtain a new value of the effective flow separation point called f'. The additional effects of a boundary layer response are incorporated as a first-order lag as given by

$$f'' = f' - D_{f_k} \tag{12}$$

where

$$D_{f_k} = D_{f_{k-1}} \exp\left(-\frac{\Delta s}{T_f}\right) + (f_k' - f_{k-1}') \exp\left(-\frac{\Delta s}{2T_f}\right) \tag{13}$$

Using the final modified separation point f'', the non-linear normal force coefficient is then obtained as

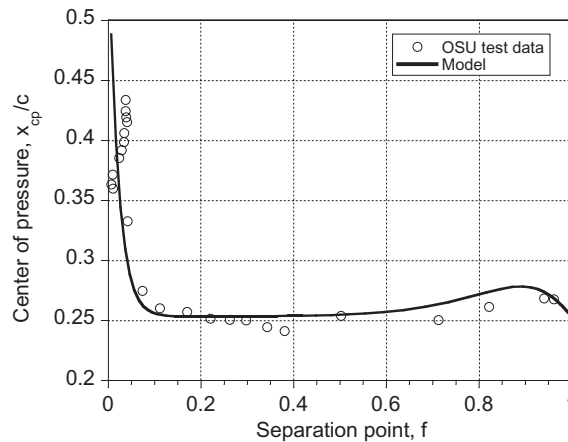$$C_n^f = C_{n_\alpha} \left(\frac{1 + \sqrt{f''}}{2} \right)^2 \sin \alpha \tag{14}$$

Figure 1. Variation of the centre of pressure with the effective trailing edge flow separation point for the S809 aerofoil
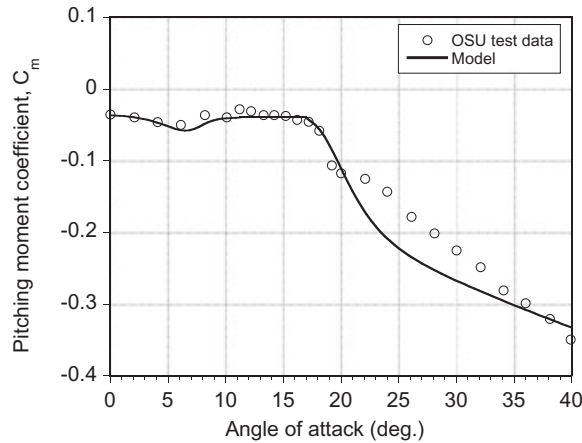
Figure 2. Variation of the pitching moment coefficient about $^1/_4$-chord with angle of attack for the S809 aerofoil

Table I. Various parameters used in the model for the S809 aerofoil

C_0	C_1	C_2	C_{m_0}	m	C_{n_1}	T_p	T_f	T_v	T_{vl}	C_{d_0}	D_f	E_f
−0·0032	−0·001	−0·025	−0·036	6	1·9	1·7	3·0	6·0	11·0	0·012	2	1

As an extension to this approach, the leading edge thrust coefficient on the aerofoil can be approximated by[12]

$$C_t = \begin{cases} C_{n_\alpha} \sqrt{f} \alpha \sin\alpha, & C_n' \le C_{n_1} \\ K_1 + C_{n_\alpha} \sqrt{f} f^\Phi \alpha \sin\alpha, & C_n' > C_{n_1} \end{cases} \tag{15}$$

Here C_n' is the so-called lagged value of the normal force and C_{n_1} is the critical normal force value. The parameter K_1 is a constant required to fit the C_t curve from 2D static test data. C_t varies as $\sqrt{f}$ below C_{n_1} and is proportional to $\sqrt{f} f^\Phi$ beyond stall. The parameter Φ is given by

$$\Phi = D_f (C_n' - C_{n_1}) + E_f (f'' - f) \tag{16}$$

where f is the quasi-static separation point, f'' is the lagged separation point at C_{n_1}, and E_f and D_f are constants given in Table I. The lift and drag coefficients are obtained by force resolution from the normal force and leading edge thrust coefficients using

$$C_l = C_n \cos\alpha + C_t \sin\alpha \tag{17}$$

$$C_d = C_n \sin\alpha - C_t \cos\alpha + C_{d_0} \tag{18}$$

where C_{d_0} is the zero-lift drag coefficient of the aerofoil.

Vortex Lift

Dynamic stall is characterized by the formation of a vortical disturbance near the leading edge of the aerofoil, which separates from the surface at some critical point and is convected downstream along the chord. The effect of the vortex shedding is accounted for in the L–B model by defining the vortex lift as the difference between the linearized value of the unsteady circulatory lift and the unsteady non-linear lift obtained from the Kirchhoff approximation, i.e. by using

$$C_n^v = C_n^c (1 - K_n) \tag{19}$$

where

$$K_n = (1 + \sqrt{f''})^2/4 \tag{20}$$

At the same time the vortex lift is allowed to decay with time, but it can be updated by a new increment in lift based on prior forcing conditions, i.e.

$$C_{n_k}^v = C_{n_{k-1}}^v \exp\left(-\frac{\Delta s}{T_v}\right) + (C_{v_k} - C_{v_{k-1}}) \exp\left(-\frac{\Delta s}{2T_v}\right) \tag{21}$$

where T_v is the vortex time decay constant. When the critical conditions for leading edge flow separation are reached (i.e. $C_n' > C_{n_1}$), the accumulated vortex lift starts to convect over the aerofoil chord. During the vortex convection process the vortex lift continues to accumulate, but it ends when the vortex reaches the aerofoil trailing edge (i.e. when the non-dimensional vortex time τ_v, is equal to the vortex traversal time T_{vl}).

The centre of pressure produced on the aerofoil also varies with the convection of the leading edge vortex over the chord and is represented by the empirical relation

$$\bar{x}_{cp_v} = 0.20\left[1 - \cos\left(\frac{\pi\tau_v}{T_{vl}}\right)\right] \tag{22}$$

The increment in pitching moment about the $\frac{1}{4}$-chord resulting from the aft movement of the centre of pressure is given by

$$C_m^v = \bar{x}_{cp_v} C_n^v \tag{23}$$

The total loading on the aerofoil is then obtained by adding the vortex induced-contributions using

$$C_n = C_n' + C_n^{nc} + C_n^v \tag{24}$$

$$C_m = C_m^c + C_m^{nc} + C_m^v \tag{25}$$

$$C_d = C_d^c + C_{d_0} \tag{26}$$

Although the above components have been described in an open loop sense, the elements are coupled, which is represented by temporary modifications of the appropriate time constants.[11] Figure 3 shows the components involved in calculating the unsteady air loads in the L–B model. The various parameters for the S809 aerofoil that were used in the modified model are given in Table I for $Re = 10^6$.

Results and Discussion

Aerodynamic coefficients of the S809 aerofoil at $Re = 10^6$ from the OSU tests[20] were used as 2D input data to determine the static stall model coefficients. Results for other Reynolds numbers have also been obtained, but this article focuses on the results for the $Re = 10^6$ case. The variation of the effective separation point f was obtained using C_n values from 2D static test data by rearranging equation (9) to solve for f. The values obtained were then fitted in a least squares sense using three exponential curves, i.e.

$$f = \begin{cases} c_1 + a_1 \exp(S_1\alpha), & \alpha \le \alpha_1 \\ c_2 + a_2 \exp(S_2\alpha), & \alpha_1 \le \alpha \le \alpha_2 \\ c_3 + a_3 \exp(S_3\alpha), & \alpha \ge \alpha_2 \end{cases} \tag{27}$$

where c_1, c_2, c_3, a_1, a_2, a_3, S_1, S_2 and S_3 are constants that depend on the Reynolds number. Table II lists the values of these constants for the S809 aerofoil at different Reynolds numbers.

The variation of the measured and reconstructed effective separation point f with angle of attack for $Re = 10^6$ is shown in Figure 4. The constants α_1 and α_2 are the angles of attack corresponding to the first and second breaks in lift curve slope. The values $\alpha_1 = 8 \cdot 2°$ and $\alpha_2 = 17 \cdot 0°$ were found to be nearly constant for the S809 aerofoil with varying Reynolds number. It can be seen that the flow separation point initially stabilizes close

Table II. Variation of curve-fitting coefficients with Reynolds number

Re	3×10^5	5×10^5	$6\cdot5 \times 10^5$	10^6
c_1	1·0	1·0	1·0	1·0
c_2	0·0	0·0	0·0	0·0
c_3	0·02	0·01	0·005	0·02
a_1	0·02539	0·00250	0·02168	0·04995
a_2	4·5278	4·5503	3·4934	2·8844
a_3	$8\cdot61 \times 10^7$	$4\cdot76 \times 10^6$	$4\cdot97 \times 10^8$	$4\cdot08 \times 10^4$
S_1	15·618	19·829	18·269	12·066
S_2	−12·499	−11·299	−11·324	−9·82694
S_3	−74·270	−64·93	−78·675	−43·0635
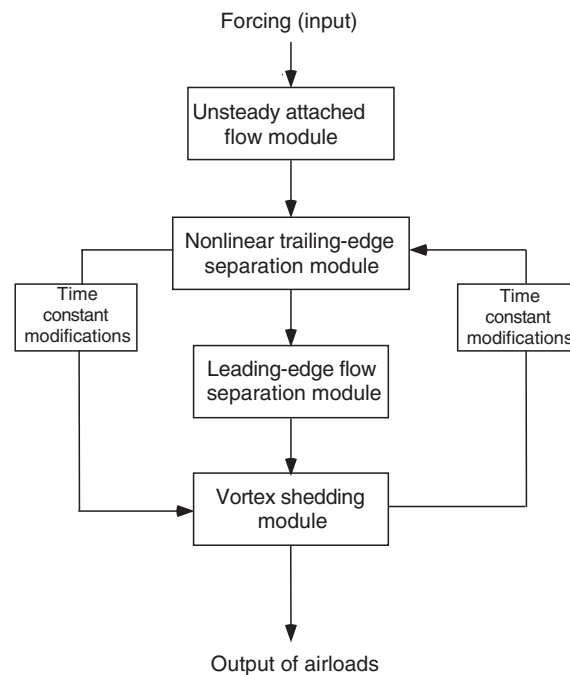
Figure 3. Flow chart of the elements of the Leishman–Beddoes dynamic stall model

to the trailing edge. With an increase in the angle of attack the flow separation point moves towards the leading edge. At very high angles of attack the separation point stabilizes near $x/c = 0\cdot02$.

The variations of the reconstructed static normal force coefficient C_n and leading edge thrust coefficient C_t are shown in Figures 5 and 6 respectively. In the attached flow region ($\alpha < \alpha_1$), good agreement was obtained with the experimental values. The range of angle of attack where C_n is essentially constant is modelled very well. In the post-stall regime, C_n is slightly underestimated at very high values of angle of attack, but it is still acceptable for engineering predictions. The agreement between the predicted and measured C_t is very good for the attached flow regime and also in the post-stall regime. However, C_t is somewhat overpredicted in the deep stall regime.

Figures 7 and 8 show the reconstructions of C_l and C_d respectively. Good agreement is obtained with experimental data at low to moderate angles of attack, whereas both the lift and drag coefficients are underpredicted at very high angles of attack. The reconstruction of the aerodynamic coefficients for the other Reynolds numbers also gave similar agreement, but for the sake of brevity only one data set has been shown here.
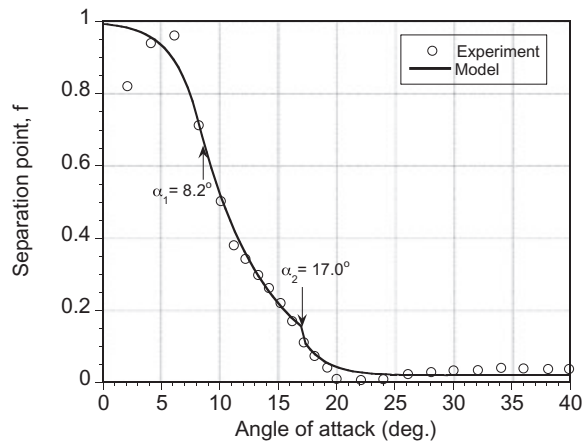
Figure 4. Variation of the effective flow separation point with angle of attack at Re = 10^6
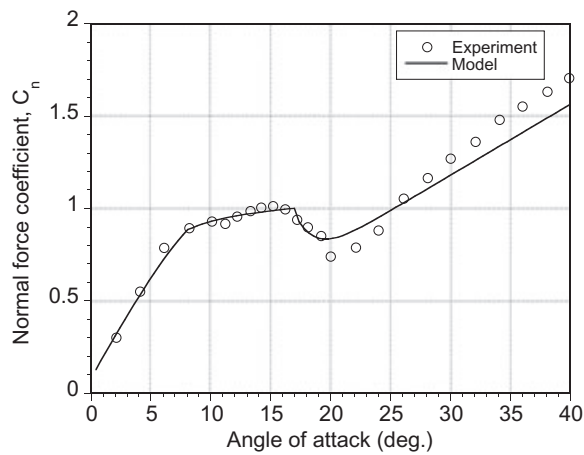

Figure 5. Variation of the measured and the predicted normal force coefficient with angle of attack at Re = 10^6
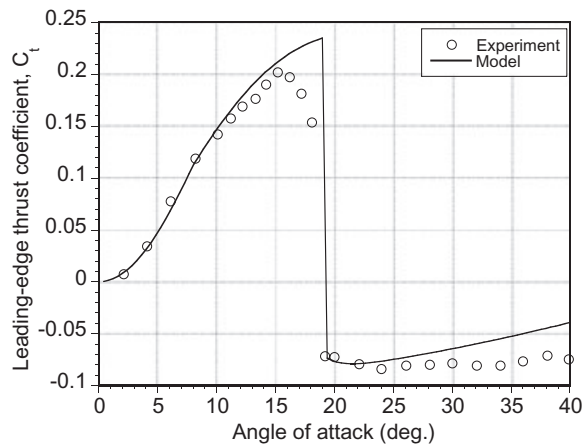

Figure 6. Variation of the measured and the predicted leading edge thrust coefficient with angle of attack at Re = 10^6
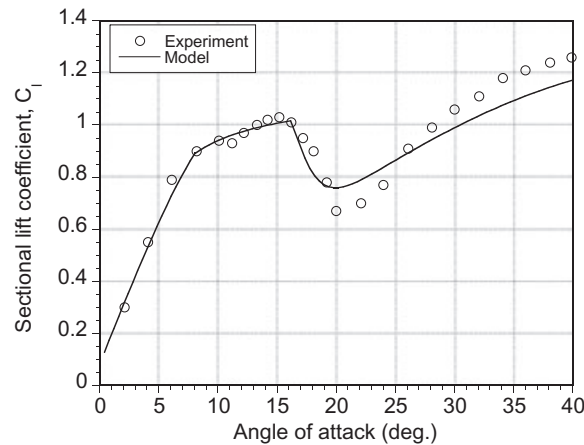
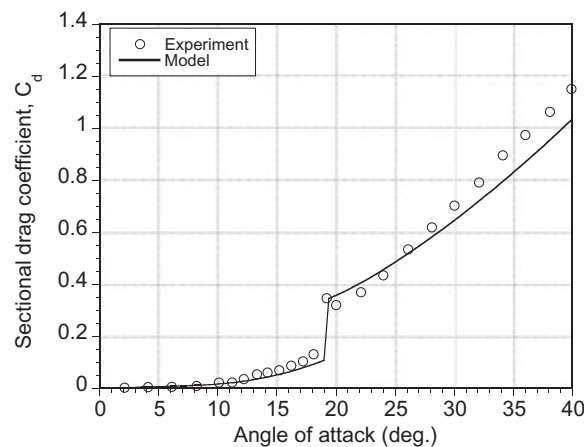*Figure 7. Variation of the measured and the predicted lift coefficient with angle of attack at* Re = 10⁶

Figure 8. Variation of the measured and the predicted drag coefficient with angle of attack at Re = 10⁶

For the unsteady case the data from the OSU tests on an oscillating S809 aerofoil at $Re = 10^6$ were used for validation.[17] The experimental data are available for sinusoidal pitch oscillations for various reduced frequencies k and mean angles of attack α_{mean} and for two angle of attack amplitudes α_{amp} of 5·5° and 10°.

The variation of the predicted lift coefficient C_l is shown in Figure 9 for reduced frequency $k = 0.026$, angle of attack amplitude $\alpha_{amp} = 5.5°$ and three values of α_{mean}. Four cycles of extracted data are plotted to show both the cycle-to-cycle repeatability as well as its variability. For mean angles of attack of 8° and 14° the hysteresis loop is predicted well by the model. Stall is delayed to a slightly higher angle of attack than in the static case, and the lift curve is almost linear up to $\alpha = 10°$. The flow reattachment process is delayed to a lower angle of attack than in the static case. For the highest mean angle of attack $\alpha_{mean} = 20°$ the experimental data show some deviations over the cycles, but the air loads are predicted well by the model on average.

The corresponding variation of C_m is shown in Figure 10. Good agreement was obtained with the experimental values for all mean angles of attack. For $\alpha_{mean} = 8°$ the flow is mostly attached and the model easily predicts C_m. For the higher values of α_{mean} the model and the experimental results show some differences. In particular, the model slightly underpredicts the angle of attack corresponding to the moment stall during the upstroke. The variation of C_d is shown in Figure 11. Again the agreement between the model and the experi-
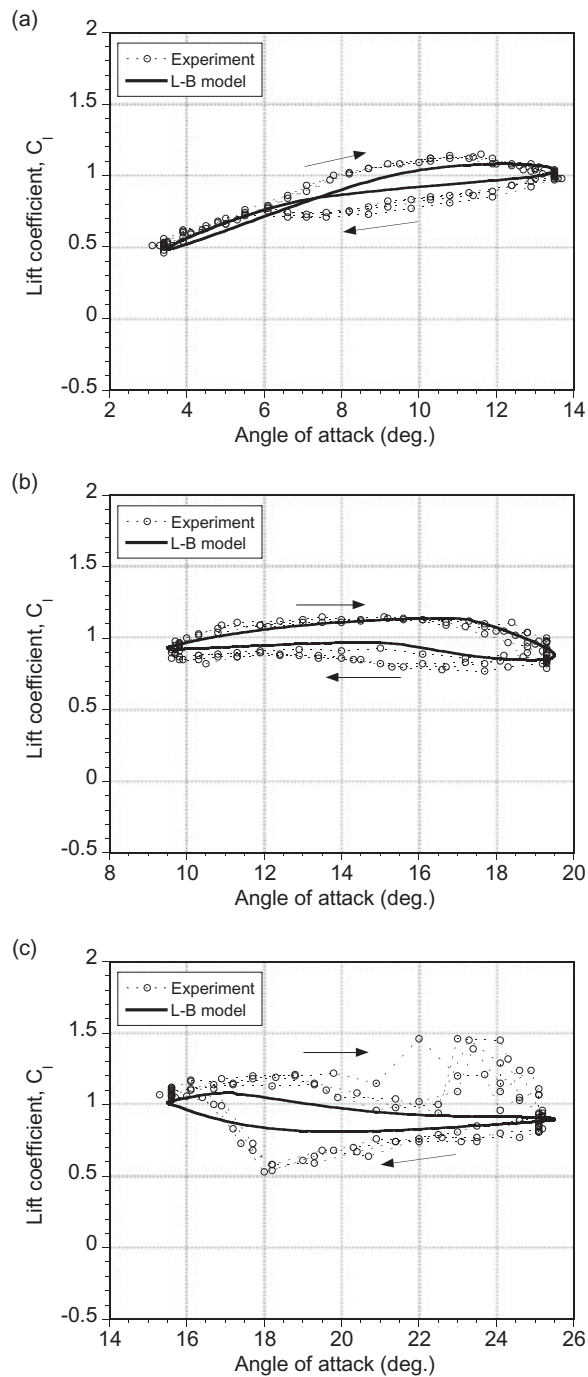
Figure 9. Variation of the lift coefficient with angle of attack for reduced frequency k = 0·026 *and angle of attack amplitude* α_{amp} = 5·5°: (a) α_{mean} = 8°; (b) α_{mean} = 14°; (c) α_{mean} = 20°
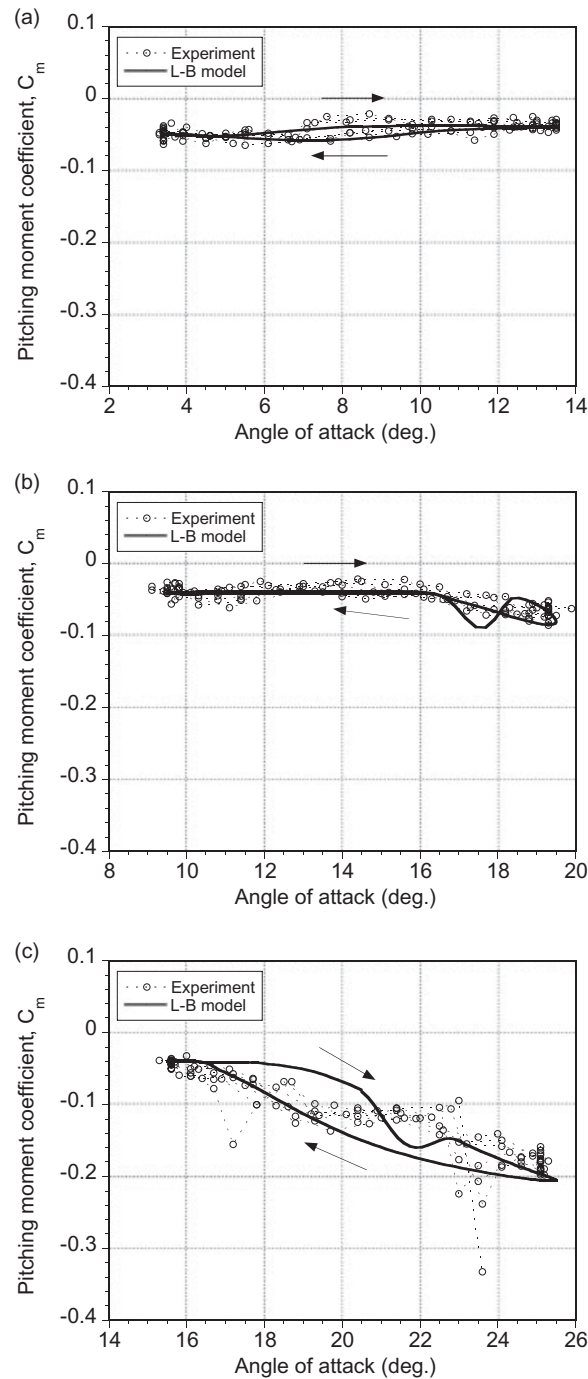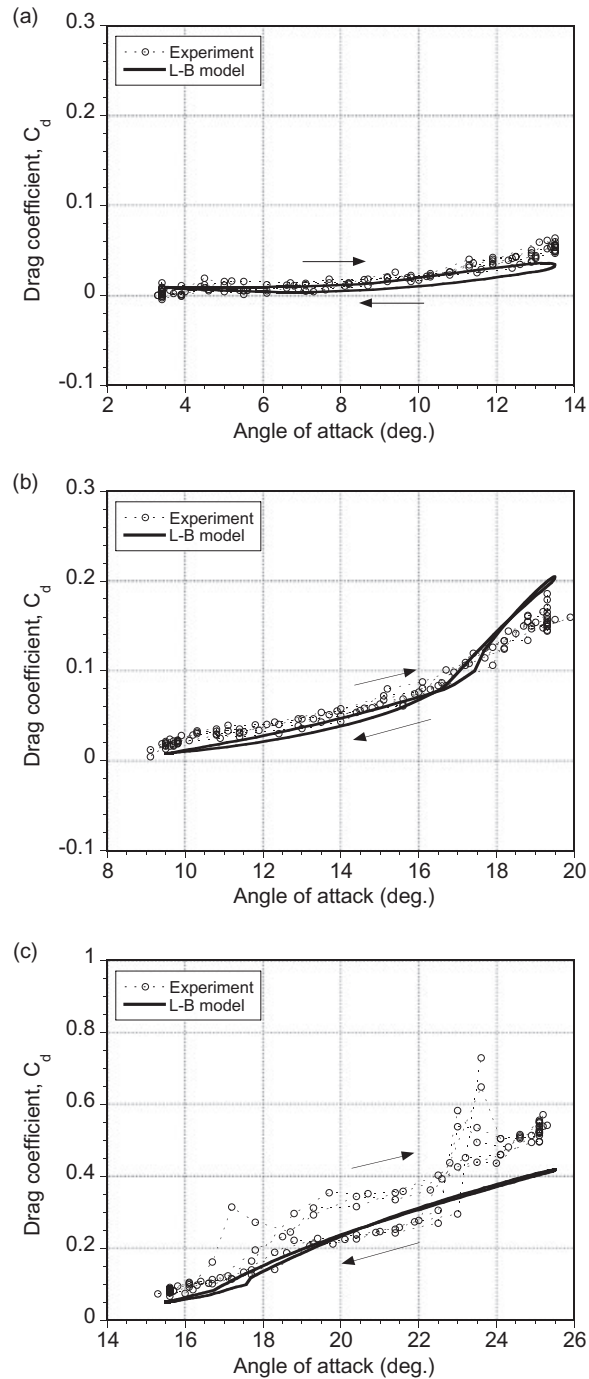
Figure 10. Variation of the pitching moment coefficient with angle of attack for reduced frequency k = 0·026 *and angle of attack amplitude* $\alpha_{amp} = 5\cdot5°$: *(a)* $\alpha_{mean} = 8°$; *(b)* $\alpha_{mean} = 14°$; *(c)* $\alpha_{mean} = 20°$

Figure 11. Variation of the drag coefficient with angle of attack for reduced frequency k = 0·026 *and angle of attack amplitude* α_{amp} = 5·5°: *(a)* α_{mean} = 8°; *(b)* α_{mean} = 14°; *(c)* α_{mean} = 20°

ment is reasonably good for $\alpha_{mean} = 8°$ and $14°$, but C_d is underpredicted for $\alpha_{mean} = 20°$. However, it should be noted that the measurements of C_d were obtained by integrating the pressure data across the thickness of the aerofoil, which is known to be very sensitive to the number of chordwise pressure points. Therefore the measurements of C_t have a higher degree of uncertainty in the deep stall regime than those of either C_n or C_m.

For the higher reduced frequencies ($k = 0.05$ and 0.077) the hysteresis in the air loads is larger than at the lowest reduced frequency, as would be expected. The agreement between the experiment and the model for C_l, C_m and C_d is reasonably good (Figures 12–17). For reduced frequency $k = 0.077$ the hysteresis behaviour in C_m was seen to be more pronounced in the experimental results compared with the predictions made by the model. The sudden decrease in C_m during moment stall is also slightly underpredicted by the model for $\alpha_{mean} = 20°$, but the overall agreement with the measurements is good enough for engineering purposes.

Measurements were also available at $Re = 10^6$ for $\alpha_{amp} = 10°$ for the same mean angles of attack and reduced frequencies as in the $\alpha_{amp} = 5.5°$ case. Figure 18 shows the variation of C_l for reduced frequency $k = 0.026$. The agreement between predictions and measurements was found to be good for low mean angles of attack. However, for the higher values of α_{mean}, some transient overshoots and undershoots were seen in the C_l measurements that were not predicted by the model. The angle of attack in the experiments also showed deviations from the prescribed nominal angle of attack history. The agreement between the experiment and C_m predictions for $k = 0.026$ (Figure 19) was again very good, as seen for $\alpha_{amp} = 5.5°$. The drag coefficient (Figure 20) was also well predicted for the lowest mean angle of attack, but it was underpredicted for $\alpha_{mean} = 14°$ and $20°$.

Figure 21 shows the variation of C_l for reduced frequency $k = 0.077$ and the three values of α_{mean}. The hysteresis in the value of C_l during the cycle is predicted reasonably well except for the flow reattachment regime, where C_l is overpredicted. For all three values of α_{mean} the variation of C_m is predicted well (Figure 22). The contribution of the dynamic stall vortex to C_m can be clearly seen for $\alpha_{mean} = 14°$ and $20°$. The variation in C_m and the pitching moment stall is predicted well with the modified L–B model. Good agreement was also achieved in the prediction of C_d (Figure 23). However, the predicted maximum drag during the cycle is lower than seen in the experimental measurements.

Conclusions

This article has presented unsteady air load predictions using the Leishman–Beddoes (L–B) unsteady stall model compared with measurements of the S809 aerofoil. Good agreement was obtained between the predictions and the experimental results for pitch oscillations at several mean angles of attack and reduced frequencies. The static aerodynamic coefficients for the S809 aerofoil were reconstructed satisfactorily by modifying the formulation originally given in the L–B model. The results showed encouraging agreement in predicting the onset and consequences of dynamic stall. The model showed slight differences in the reattachment phase during downstroke, which could be improved. The model was successful in predicting the dynamic stall characteristics of the S809 aerofoil with almost same dynamic time constants as were used in the original L–B model. It has been shown that, with a proper representation of the static stall characteristics, this model can be used to predict dynamic stall for aerofoil sections typical of those used for wind turbine applications.
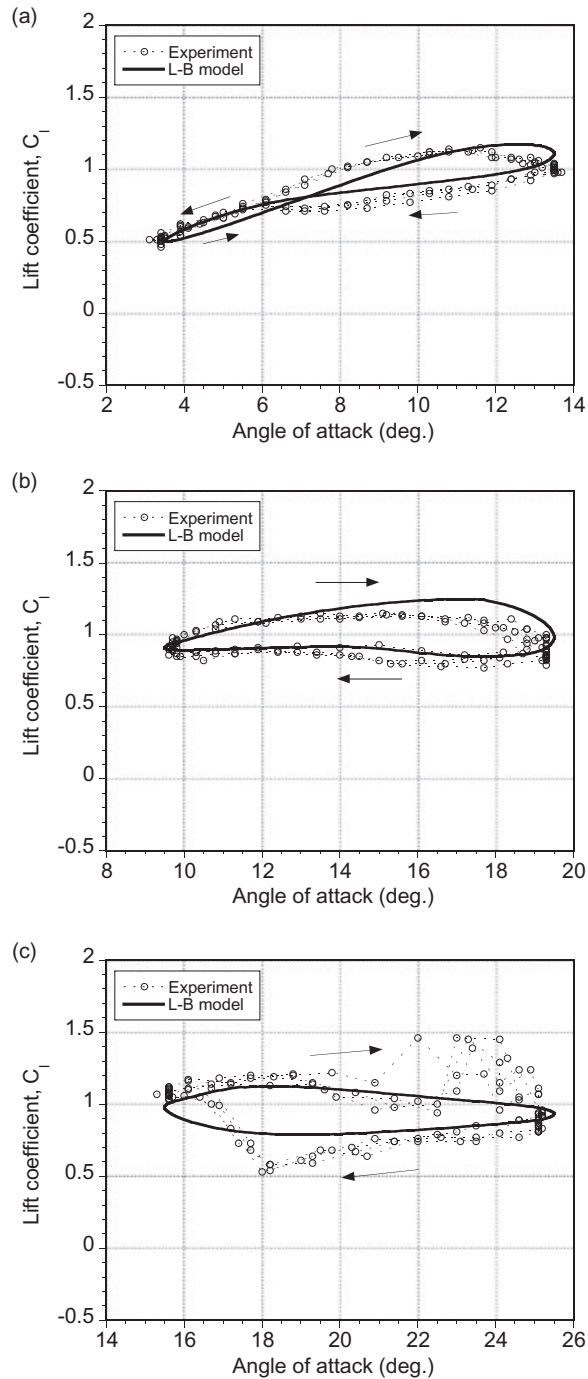
Acknowledgements

Figure 12. *Variation of the lift coefficient with angle of attack for reduced frequency* k = 0·05 *and angle of attack amplitude* $\alpha_{amp} = 5\cdot5°$: *(a)* $\alpha_{mean} = 8°$; *(b)* $\alpha_{mean} = 14°$; *(c)* $\alpha_{mean} = 20°$
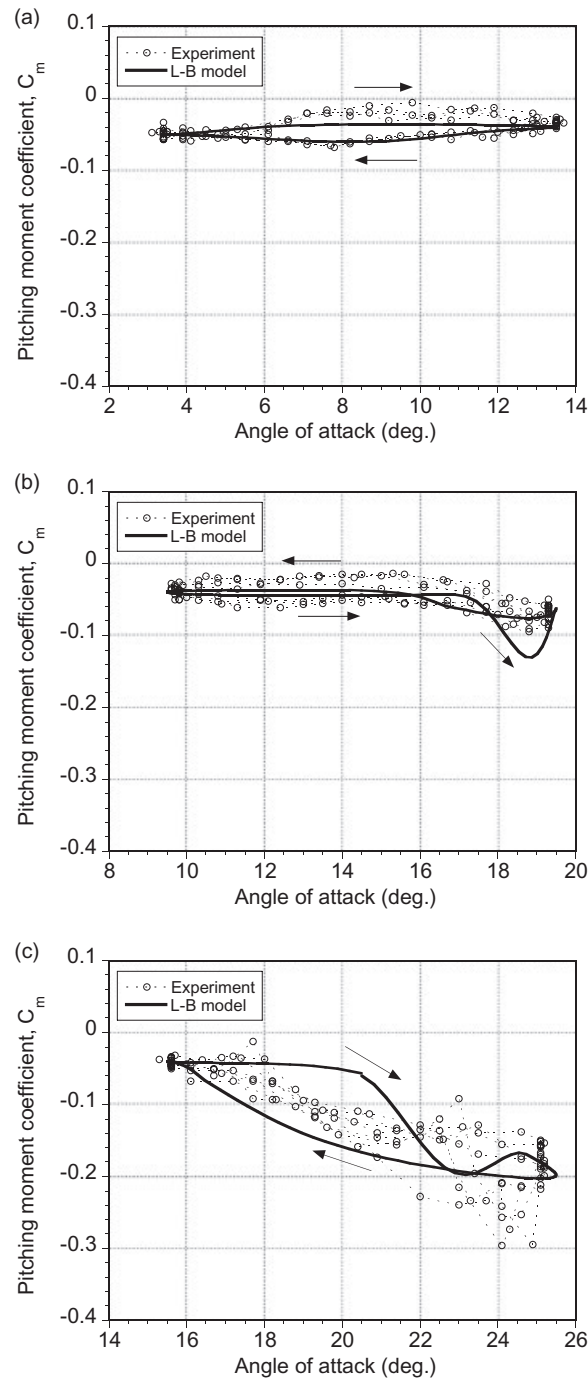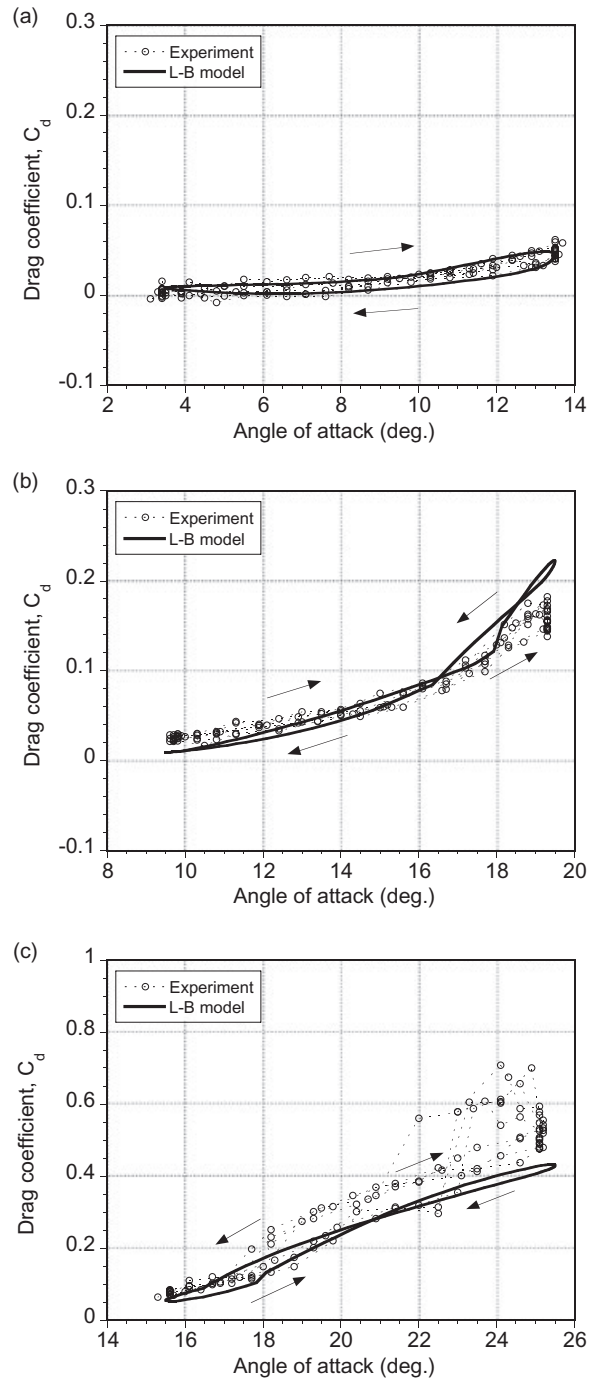
Figure 13. *Variation of the pitching moment coefficient with angle of attack for reduced frequency* k = 0·05 *and angle of attack amplitude* α_{amp} = 5·5°: (a) α_{mean} = 8°; (b) α_{mean} = 14°; (c) α_{mean} = 20°
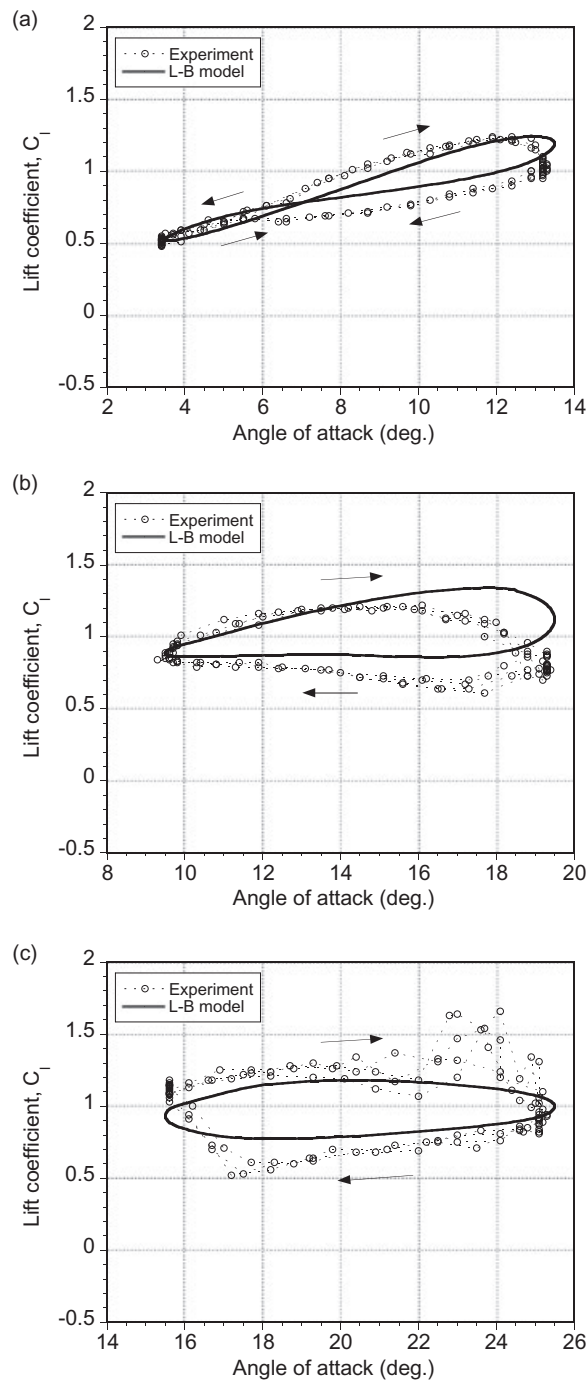
Figure 14. Variation of the drag coefficient with angle of attack for reduced frequency k = 0·05 *and angle of attack amplitude* α_{amp} = 5·5°: (a) α_{mean} = 8°; (b) α_{mean} = 14°; (c) α_{mean} = 20°

Figure 15. Variation of the lift coefficient with angle of attack for reduced frequency k = 0·077 *and angle of attack amplitude* α_{amp} = 5·5°: *(a)* α_{mean} = 8°; *(b)* α_{mean} = 14°; *(c)* α_{mean} = 20°
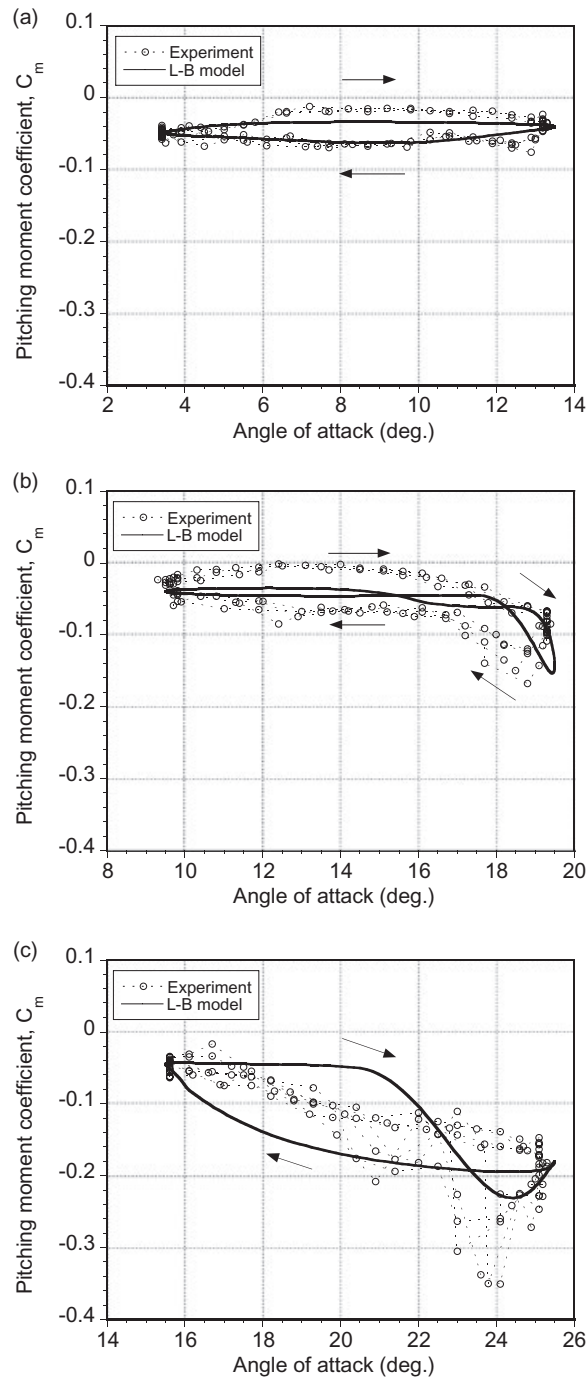
Figure 16. Variation of the pitching moment coefficient with angle of attack for reduced frequency k = 0·077 *and angle of attack amplitude* $\alpha_{amp} = 5\cdot5°$: *(a)* $\alpha_{mean} = 8°$; *(b)* $\alpha_{mean} = 14°$; *(c)* $\alpha_{mean} = 20°$
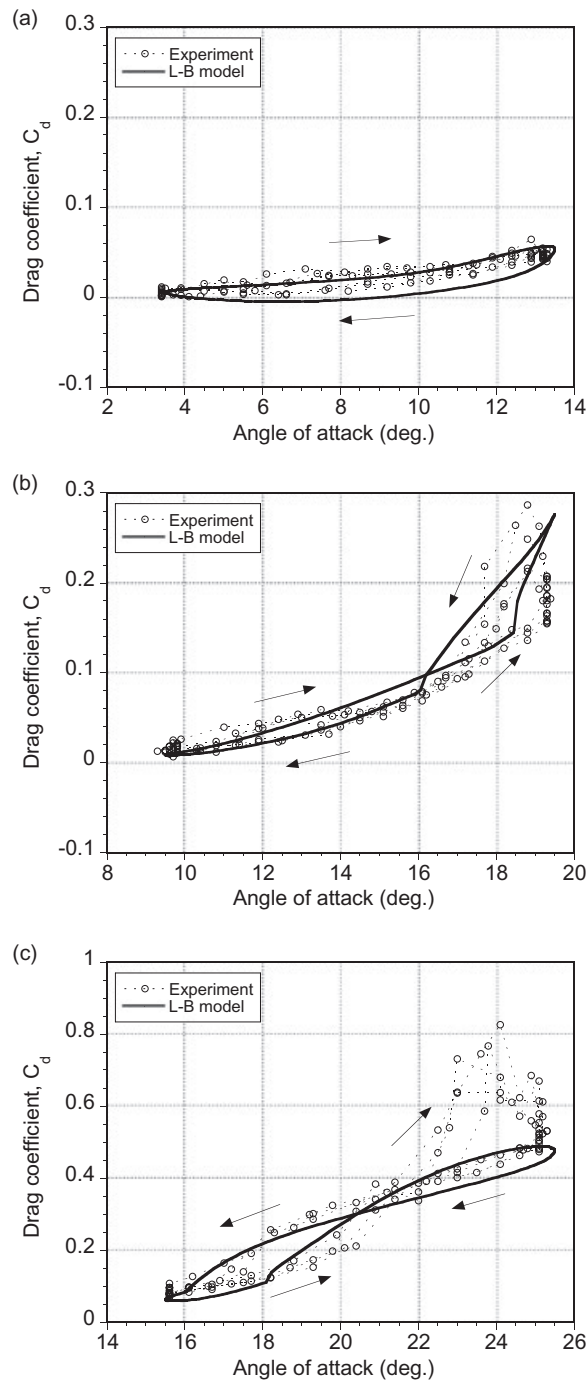
Figure 17. Variation of the drag coefficient with angle of attack for reduced frequency k = 0·077 *and angle of attack amplitude* α_{amp} = 5·5°: *(a)* α_{mean} = 8°; *(b)* α_{mean} = 14°; *(c)* α_{mean} = 20°
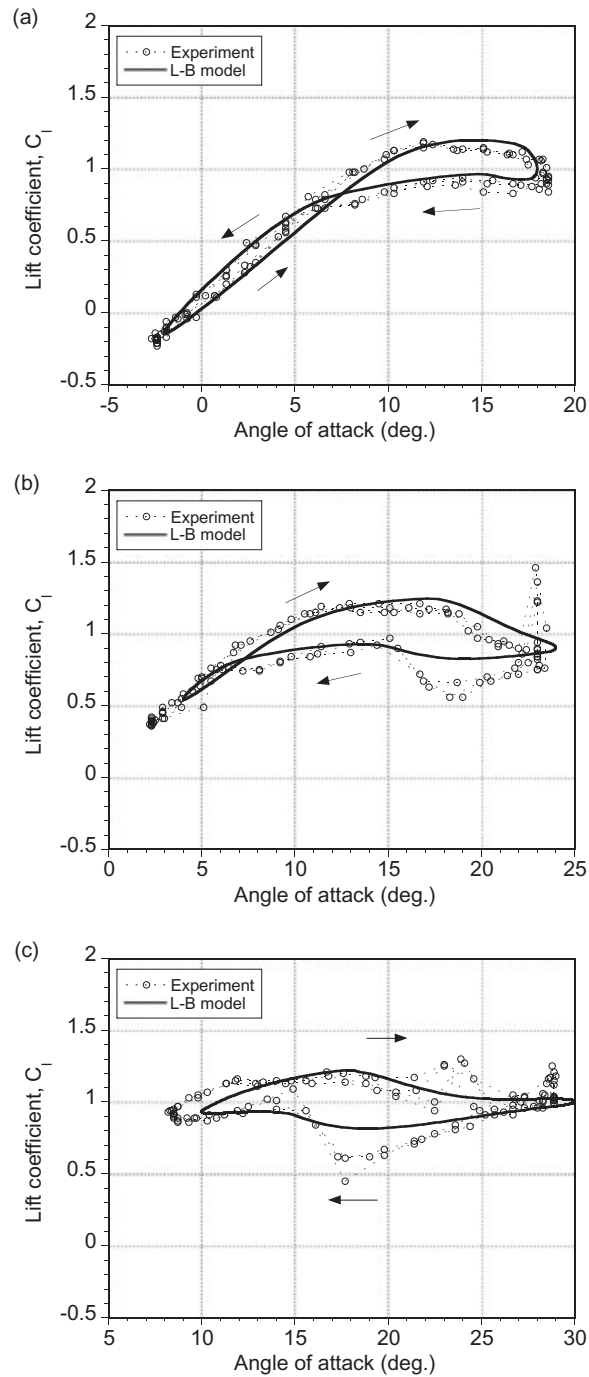
Figure 18. Variation of the lift coefficient with angle of attack for reduced frequency k = 0·026 *and angle of attack amplitude* $\alpha_{amp} = 10°$; (a) $\alpha_{mean} = 8°$; (b) $\alpha_{mean} = 14°$; (c) $\alpha_{mean} = 20°$
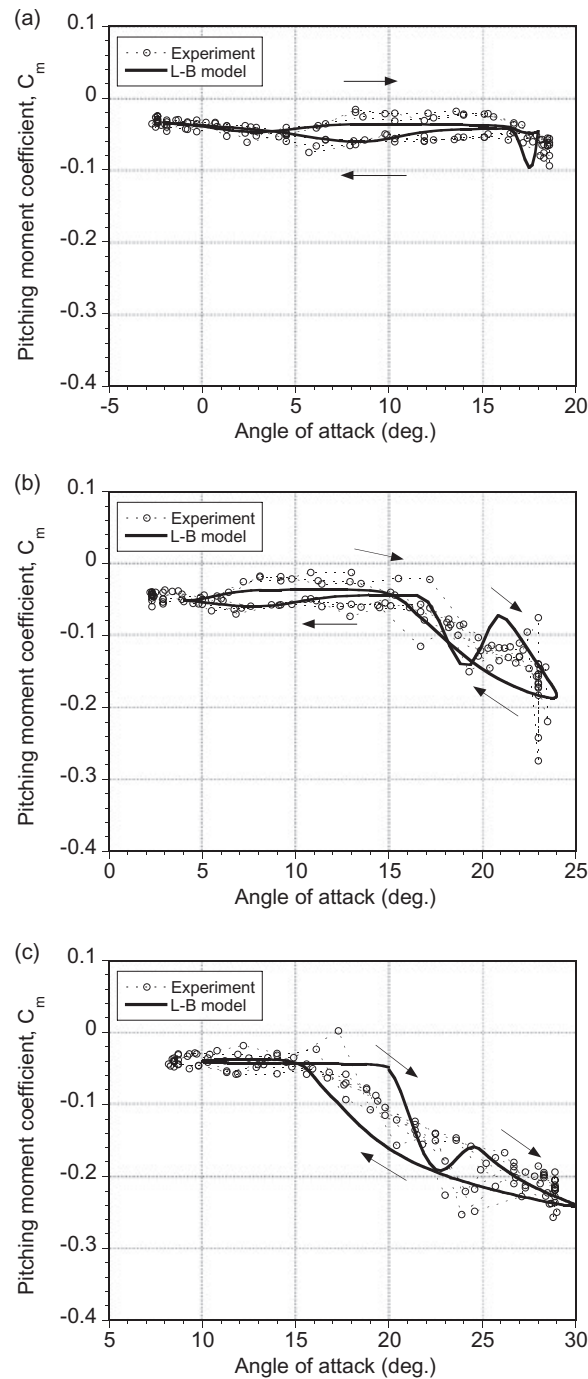
Figure 19. Variation of the pitching moment coefficient with angle of attack for reduced frequency k *= 0·026 and angle of attack amplitude* α_{amp} *= 10°: (a)* α_{mean} *= 8°; (b)* α_{mean} *= 14°; (c)* α_{mean} *= 20°*

Figure 20. Variation of the drag coefficient with angle of attack for reduced frequency k *= 0·026 and angle of attack amplitude* α_{amp} *= 10°: (a)* α_{mean} *= 8°; (b)* α_{mean} *= 14°; (c)* α_{mean} *= 20°*
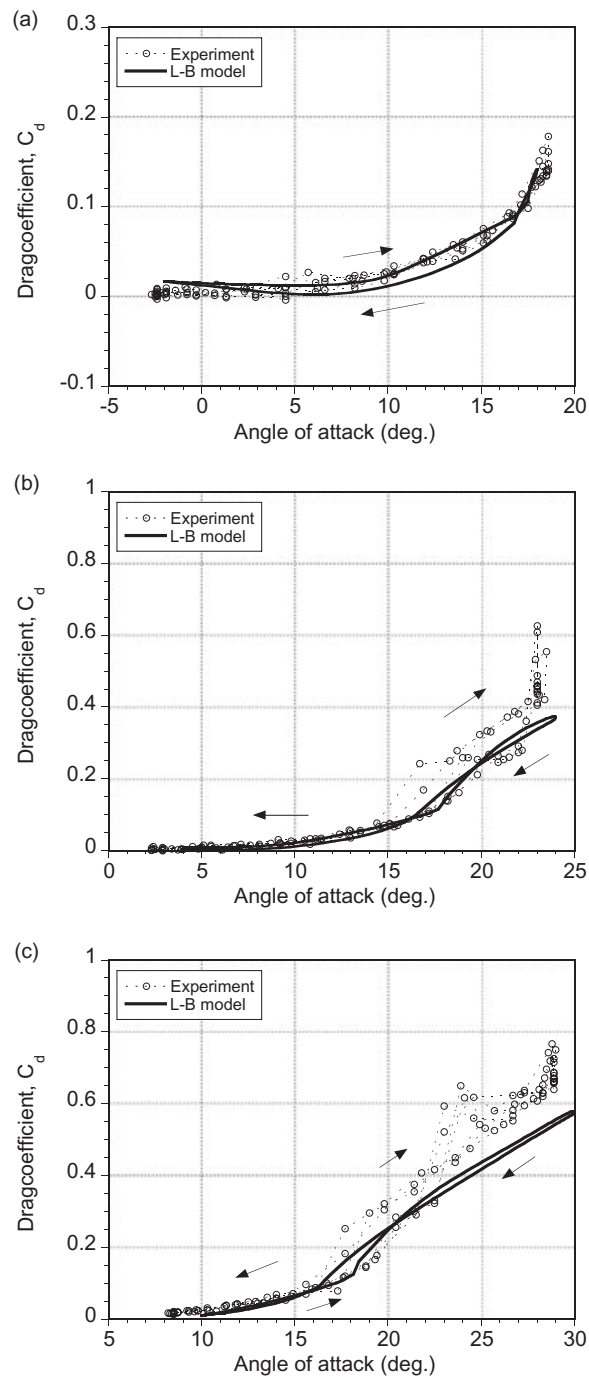
Figure 21. Variation of the lift coefficient with angle of attack for reduced frequency k = 0·077 *and angle of attack amplitude* α_{amp} = 10°: *(a)* α_{mean} = 8°; *(b)* α_{mean} = 14°; *(c)* α_{mean} = 20°

Figure 22. Variation of the pitching moment coefficient with angle of attack for reduced frequency k = 0·077 *and angle of attack amplitude* α_{amp} = 10°: *(a)* α_{mean} = 8°; *(b)* α_{mean} = 14°; *(c)* α_{mean} = 20°
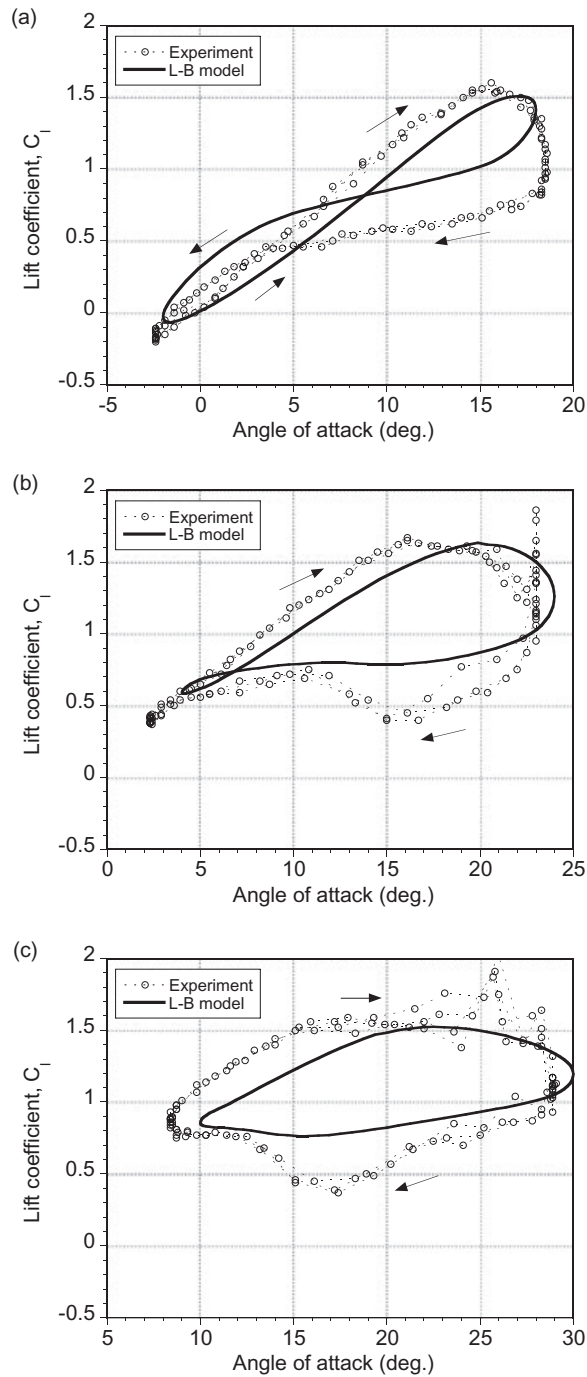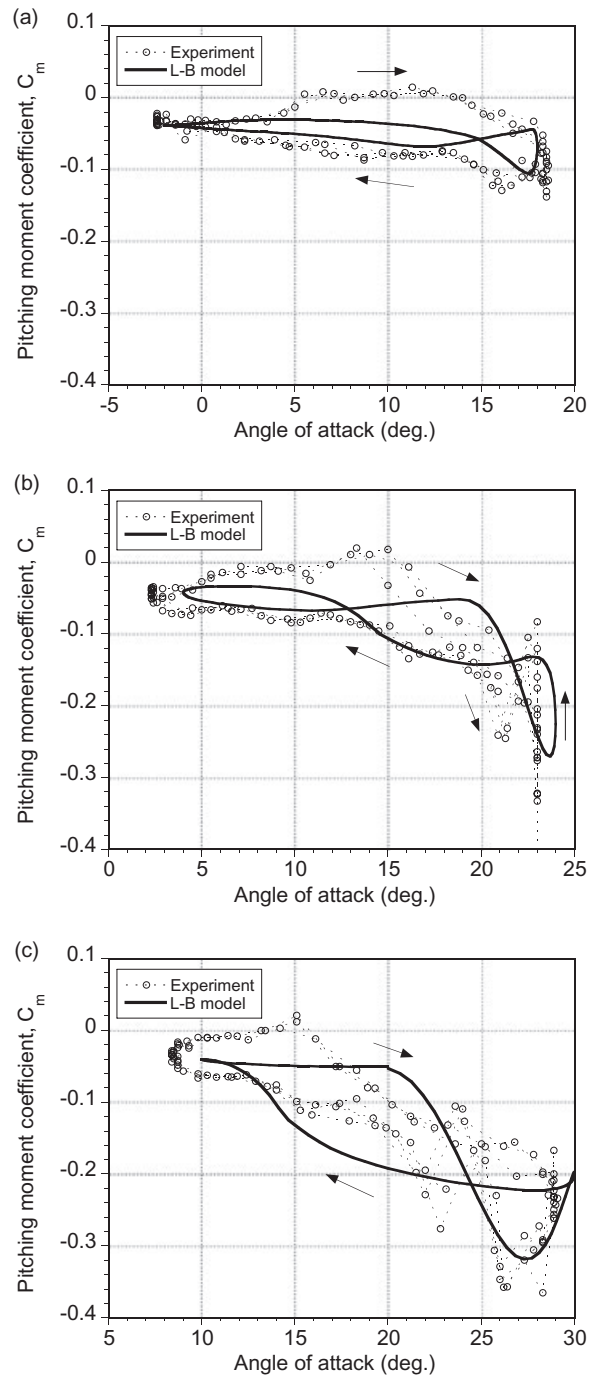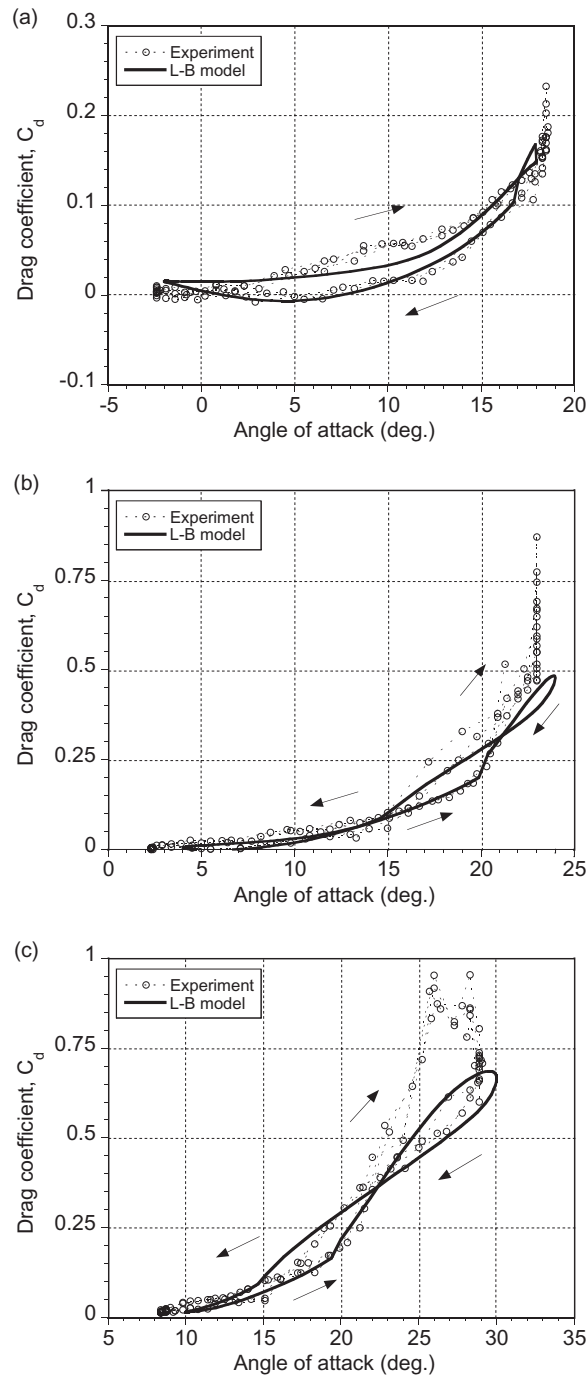
Figure 23. Variation of the drag coefficient with angle of attack for reduced frequency k = 0·077 *and angle of attack amplitude* α_{amp} = 10°: *(a)* α_{mean} = 8°; *(b)* α_{mean} = 14°; *(c)* α_{mean} = 20°

Appendix: Nomenclature

c	aerofoil chord (m)
C_0	mean offset of the aerodynamic centre from the $\frac{1}{4}$-chord
C_1, C_2	coefficients for non-linear variation of the centre of pressure
C_d	drag coefficient
C_{d_0}	zero-lift drag coefficient
C_l	lift coefficient
C_m	pitching moment coefficient
C_{m_0}	zero-lift pitching moment coefficient
C_m^v	vortex-induced pitching moment coefficient
C_n	normal force coefficient
C_n'	normal force coefficient including pressure lag response
C_n^c	circulatory normal force coefficient
C_n^f	normal force coefficient including trailing edge separation
C_n^p	normal force coefficient under potential flow conditions
C_n^v	vortex-induced normal force coefficient
C_{n_1}	critical normal force coefficient
C_{n_α}	normal force curve slope
C_t	leading edge thrust coefficient
D_f, D_p	deficiency functions
f	effective flow separation point
f''	flow separation point including unsteady boundary layer response
k	reduced frequency, $\omega c / 2V_\infty$
M	Mach number
q	non-dimensional pitch rate, $\dot{\alpha} c / V_\infty$
Re	Reynolds number, $\rho V_\infty c / \mu$
t	time (s)
T_f, T_p, T_v	time constants (semi-chords)
T_{v_1}	vortex traversal time
s	non-dimensional distance travelled by aerofoil in semi-chords, $2V_\infty t / c$
V_∞	free stream velocity (m s^{-1})
x	distance along the chord (m)
x_{ac}	aerodynamic centre (m)
x_{cp}	centre of pressure (m)
$\bar{x}_{cp_v}$	non-dimensional vortex-induced centre of pressure
α	geometric angle of attack (rad)
α_1	angle of attack corresponding to first break in lift (rad)
α_2	angle of attack corresponding to second break in lift (rad)
α_{amp}	angle of attack amplitude (rad)
α_{mean}	mean angle of attack (rad)
α_f	effective angle of attack with pressure lag (rad)
$\dot{\alpha}$	pitch rate (rad s^{-1})
β	Prandtl–Glauert compressibility factor, $\sqrt{1-M^2}$
ρ	density (kg m^{-3})
μ	viscosity (kg m^{-1} s^{-1})
τ_v	non-dimensional vortex time
ω	circular frequency (rad s^{-1})

References

1. Leishman JG. Challenges in modeling the unsteady aerodynamics of wind turbines. *Wind Energy* 2002; **5**: 86–132.
2. Snel H. Review of the wind turbine aerodynamics. *Wind Energy* 2003; **6**: 203–132.
3. Hansen AC, Butterfield CP. Aerodynamics of horizontal-axis wind turbines. *Annual Review of Fluid Mechanics* 1993; **25**: 115–149.
4. Fingersh LJ, Simms D, Hand M, Jager D, Cotrell J, Robinson M, Schreck S, Larwood S. Wind tunnel testing of NREL's unsteady aerodynamics experiment. *Proceedings of 20th ASME Wind Energy Symposium and 39th AIAA Aerospace Sciences Meeting*, Reno, NV, 2001; 194–200.
5. Wang T, Coton FN. A high resolution tower shadow model for downwind turbines. *Journal of Wind Engineering and Industrial Aerodynamics* 2001; **89**: 873–892.
6. McCroskey WJ, Carr LW, McAlister KW. Dynamic stall experiments on oscillating airfoils. *AIAA Journal* 1967; **14**: 57–63.
7. Rasmussen R, Petersen JT, Madsen HA. Dynamic stall and aerodynamic damping. *ASME Journal of Solar Energy Engineering* 1999; **121**: 150–155.
8. Duque EPN, van Dam CP, Drodeur RR, Chao DD. Navier–Stokes analysis of time-dependent flows about a wind turbine. *Proceedings of 3rd ASME/JSME Joint Fluids Engineering Conference*. San Francisco, CA, 1999.
9. Johansen J, Sorenson NN, Michelsen JA, Schreck S. Detached-eddy simulation of flow around the NREL Phase-VI blade. *Wind Energy* 2002; **5**: 185–197.
10. Beddoes TS. Representation of aerofoil behaviour. *Vertica* 1983; **7**: 183–197.
11. Leishman JG, Beddoes TS. A generalized method for unsteady airfoil behavior and dynamic stall using the indicial method. *Proceedings of 42nd Annual Forum of the American Helicopter Society.* Washington, DC, 1986; 243–265.
12. Leishman JG, Beddoes TS. A semi-empirical model for dynamic stall. *Journal of the American Helicopter Society* 1989; **34**(3): 3–17.
13. Tran CT, Pitot D. Semi-empirical model for the dynamic stall of airfoils in view of the application to the calculation of the responses of a helicopter blade in forward flight. *Vertica* 1981; **5**: 35–53.
14. Leishman GJ. *Principles of Helicopter Aerodynamics.* Cambridge University Press: Cambridge, 2000; 390–392.
15. Pierce K, Hansen AC. Prediction of wind turbine rotor loads using the Beddoes–Leishman model for dynamic stall. *Journal of Solar Energy Engineering* 1995; **117**: 200–204.
16. Voutsinas SG, Riziotis VA, Dimitris DG, Chaviaropoulos PK. Profile stall characteristics, aerodynamic damping and design implications for wind turbine blades. *Proceedings of 18th ASME Wind Energy Symposium and 37th AIAA Aerospace Sciences Meeting.* Reno, NV, 1999; 314–324.
17. Ramsay RR, Hoffman MJ, Gregorek GM. Effects of grit roughness and pitch oscillations on the S809 airfoil. *Technical Report TP-442-7817*, NREL, Golden, CO, 1995.
18. Leishman JG, Bhagwat MJ, Bagai A. Free-vortex filament methods for the analysis of helicopter rotor wakes. *Journal of Aircraft* 2003; **39**: 759–775.
19. Gupta S, Leishman JG. Stability of methods in the free-vortex wake analysis of wind turbines. *Proceedings of 23rd ASME Wind Energy Symposium and 42nd AIAA Aerospace Sciences Meeting.* Reno, NV, 2004; 339–353.
20. Hand MM, Simms DA, Fingersh LJ, Jager DW, Cortell JR, Schreck S, Larwood SM. Unsteady aerodynamics experiment Phase VI: wind tunnel test configurations and available data campaigns. *Technical Report TP-500-29955*, NREL, Golden, CO, 2001.
21. McCroskey WJ, McAlister KW, Carr LW, Pucci SL. An experimental study of dynamic stall on advanced airfoil sections. *NASA TM-84245*, vols 1–3, 1982.
22. Thwaites B. *Incompressible Aerodynamics.* Dover: New York, NY, 1987.
23. Gupta S, Leishman JG. Stall modeling of a parked wind turbine blade and comparison with experiment. *Proceedings of 24th ASME Wind Energy Symposium and 43rd AIAA Aerospace Sciences Meeting.* Reno, NV, 2005; 227–246.